International Forum on Aeroelasticity and Structural Dynamics
IFASD 2022
13-17 June 2022, Madrid, Spain

AN INTEGRATED FLEXIBLE AIRCRAFT MODEL FOR OPTIMAL CONTROL SURFACE SCHEDULING OF MANOEUVRE LOAD ALLEVIATION AND WING SHAPE CONTROL FUNCTIONS

Thiemo M. Kier[1]

[1]DLR, German Aerospace Center
Institute of System Dynamics and Control
82234 Weßling, GERMANY
Thiemo.Kier@dlr.de

Abstract: In the field of structural loads analysis, the focus is on accurate modelling of the lift forces, as they are the main driver of the structural sizing loads. Hence, in many aeroelastic implementations, forces acting in the longitudinal direction of the airframe are neglected. However, for flight mechanical assessments and cruise performance, the forces in the direction of the flow are essential. This issue can be addressed by either using higher fidelity methods or by extension of the potential flow based methods to account for longitudinal forces such as the induced drag.

A common practice is to pass the deformations of the structural model to the aerodynamic code and vice versa the pressure loading is passed to the structural code, which in turn is used to solve the flight dynamics equations of motion followed by a aircraft trimming procedure. This paper proposes an extension of the Vortex Lattice Method (VLM) implementation used in classical loads analysis. The resulting closed-form integral model allows for a fast execution without tedious iterations between the interfacing disciplinary codes.

The present implementation of the VLM accounts for the inherently nonlinear behavior of the induced drag and the dependence on the on-flow direction, while preserving the Aerodynamic Influence Coefficients and boundary conditions in matrix form, compatible with classical formulations.

The integral aircraft model is then used for wing shape control by optimizing the control surface scheduling of the trimmed, flexible aircraft to minimize the induced drag in off-design flight conditions. Another important objective is to minimize the wing bending moments during pull up manoeuvres to reduce the sizing loads and the resulting structural weight of the wing. These optimized control surfaces deflections constitute the allocation for the Manoeuvre Load Alleviation (MLA) control function. Furthermore, the inclusion of induced drag allows also for a better representation of the characteristics of the flight dynamics such as the phugoid motion, which in turn affects the design of the baseline flight controller.

The optimizations of the control surface deflections regarding wing shape and manoeuvre load alleviation control will be exemplified with a model of the FLEXOP aircraft, a high aspect ratio subscale demonstrator equipped with multiple trailing edge control surfaces.

1 INTRODUCTION

For many aircraft design analyses, mathematical models need to be evaluated numerous times, either to reflect changes during the design process or to evaluate certain criteria in the entire

flight envelope. Therefore, loop capable models are essential which are fast to simulate, yet accurate enough for the specific analysis purpose.

A modelling approach for such applications was proposed in [1]. In [2] this modelling approach was used to optimize lift distributions for manoeuvre load and gust load alleviation. The in-plane forces for important flight dynamics and drag reduction were accounted for by the use of 3D panel methods [3–5]. In this paper, the integrated model has been improved to also support analyses regarding performance by accounting for induced drag forces with the Vortex Lattice Method. The current paper also features application examples pertaining to active manoeuvre load alleviation as well as performance improvement through optimization of the lift distributions for an high aspect ratio flexible aircraft configuration with multiple wing trailing edge flaps.

Optimal control surface scheduling to minimized drag of an elastic aircraft has been demonstrated in [6], which relies on a far field Trefftz plane analysis to evaluate the induced drag. An experimental test case was shown in [7], where a wind tunnel model of a flexible wing was used to validate the numerical model. This numerical model coupled a structural beam and a 3D potential flow panel method with an iterative scheme. In [8] a Vortex Lattice Method was used in combination with a 2D airfoil aerodynamic code to account for transonic and viscous effects. The aeroelastic and trim effects were regarded by iterations between structural deformation and aerodynamic lift distribution. A method for dynamic allocation for gust load alleviation is described in [9] with respect to optimal control surface scheduling for active load control.

The present aerodynamic model is based on a near field extension of the Vortex Lattice Method as commonly used for aerodynamic analyses. Instead of using an iterative exchange between the structural and aerodynamic model, the present method uses a matrix based formulation, which allows a closed form integral model formulation. This way, nonlinear effects like in-plane aerodynamic forces and induced drag components can be captured efficiently.

2 MODELLING APPROACH

The following section summarizes the general principles regarding the integration aspects of the flexible aircraft analysis model, i.e. the equations of motion and the external forcing due to propulsion and aerodynamics. A particular focus is on the treatment of the nonlinear quasi-steady aerodynamics and the derivation of the extended Vortex Lattice Method with application of the boundary conditions in matrix form. These described equations have been integrated in the loads environment VarLoads [10], with which all the subsequent simulation results have been obtained.

2.1 Quasi-Steady Aerodynamics: Vortex Lattice Method

As pointed out before, the large amount of design analysis cases that have to be considered in many aircraft design disciplines are still prohibitive for a wide spread adoption of costly CFD-CSM coupled calculations. Therefore, usually classical methods derived from potential theory, such as the Vortex Lattice Method (VLM) [11] are still in use for many applications regarding flexible aircraft dynamics.

The Vortex Lattice Method (VLM) discretizes a lifting surface by trapezoidal shaped elementary wings, so called aerodynamic boxes. The aerodynamic lift is generated by placing a vortex along the quarter chord line of such an aerodynamic box. According to the Helmholtz theorems, such a vortex must either end at a solid surface, or extend to infinity. Hence, the bound vortex

is extended at both corner points to infinity, forming the well known horseshoe shape with its legs pointing in free stream direction. The circulation strengths $\mathbf{\Gamma}_j$ of the individual horseshoe vortices are then determined by the Biot-Savart-Law and by meeting the flow compatibility condition, i.e. no perpendicular flow $\mathbf{v}_j$ through the solid surface at the control points at $3/4$ chord, according to Pistolesi's theorem [12].

$$\mathbf{v}_j = \mathbf{A}_{jj}\mathbf{\Gamma}_j \tag{1}$$

Figure 1 depicts the geometry of an aerodynamic box. The load acting point is located at mid span, quarter chord ($l-$ set) and the control point at three quarter ($j-$ set) chord point, respectively. The box reference point ($k-$ set) is at the center of the box. The panel chord is c_j and the span is b_j. The vector of the bound vortex is denoted by $\mathbf{b}_l$.

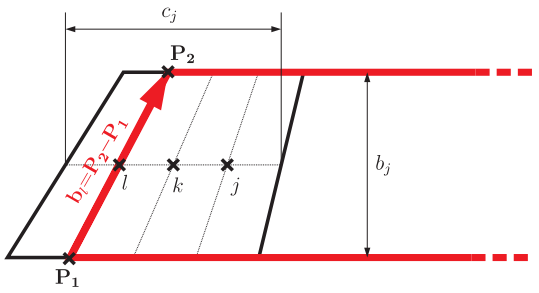

Figure 1: Geometrical properties of an aerodynamic box

The Kutta-Joukowski-Law relates the circulation to the lifting force.

$$L_j = \rho U_\infty \Gamma_j b_j \tag{2}$$

Normalizing the velocities at the control point $\mathbf{w}_j = \frac{\mathbf{v}_j}{U_\infty}$ and inversion of (1), yields the differential pressure coefficients with the aerodynamic AIC matrix.

$$\Delta\mathbf{c}_{\mathbf{p}_j} = \mathbf{Q}_{jj}\mathbf{w}_j \tag{3}$$

Reversely, the circulation of an individual horseshoe vortex can be calculated from the pressure coefficient as follows.

$$\Gamma_j = U_\infty \frac{c_j}{2} \Delta c_{p_j} \tag{4}$$

This is the "classical" implementation of the VLM as employed for instance in the aeroelastic solutions of `NASTRAN` [13]. In the degree of freedom (DOF) notation for the j,k, and l set this implies :

$$\mathbf{u}_j = \begin{bmatrix} z \end{bmatrix}_j \;;\; \mathbf{u}_k = \begin{bmatrix} z & \theta \end{bmatrix}_k^{\mathrm{T}} \;;\; \mathbf{u}_l = \begin{bmatrix} z \end{bmatrix}_l \tag{5}$$

The boundary condition has to be met at $3/4$ chord location in z-direction ($j-$set). The resulting lift in the $l-$ set also acts in z-direction wrt the box geometry at the quarter chord, resulting in an additional moment about the y axis when regarding the box reference location $k-$ set.

Alternatively, the Kutta-Joukowski-Law can be cast in the following form, involving a cross product instead of a scalar multiplication. This approach was proposed in [14] to enhance the flexible aircraft models for load analysis.

$$\mathbf{L}_l = \rho \mathbf{V}_l \times (\mathbf{b}_l \Gamma_j) \quad \text{with } \mathbf{L}_l, \mathbf{V}_l, \mathbf{b}_l \in \mathbb{R}^3 \text{ and } \Gamma_j \in \mathbb{R}^1 \tag{6}$$

The vector $\mathbf{b}_l$ is the vector quantity between the two corners of the horseshoe vortex, i.e. the bound vortex. The lift force $\mathbf{L}_l$ then acts, as aerodynamic theory predicts, perpendicular to the local stream velocity $\mathbf{V}_l$ at the quarter chord point. Consequently the DOF-set have to be extended:

$$\mathbf{u}_j = \begin{bmatrix} z \end{bmatrix}_j \; ; \; \mathbf{u}_k = \begin{bmatrix} x & y & z & \varphi & \theta & \psi \end{bmatrix}_k^{\mathrm{T}} \; ; \; \mathbf{u}_l = \begin{bmatrix} x & y & z \end{bmatrix}_l^{\mathrm{T}} \tag{7}$$

The lift at the quarter chord ($l-\mathrm{set}$) is now a vector quantity in all three translational directions. The $k-\mathrm{set}$ at the reference point was extended to all six DOF to account for moments arising from the directional lift.

Equation (6) can now be recast in matrix form by using eq. (4) and the skew matrix operator $\mathbf{sk}()$ for the cross product.

$$\mathbf{L}_l = q_\infty \left(\begin{bmatrix} -\mathbf{sk}(\mathbf{b}_l) \end{bmatrix} \mathbf{w}_l \right) \odot \left(c_j \begin{bmatrix} 1 & 1 & 1 \end{bmatrix}^{\mathrm{T}} \Delta c_{p_j} \right) \tag{8}$$

The vector $\mathbf{w}_l$ is the velocity at quarter chord normalized by the free stream velocity. On individual box level, the quantities with index l are elements in $\mathbb{R}^3$, whereas index j denotes elements in $\mathbb{R}^1$. The operator $\odot$ in eq. (8) refers to an elementwise multiplication. A blockdiagonal extension of eq. (8) allows the use of the full DOF vectors in the $l-$ respectively $j-\mathrm{set}$. Since both $\mathbf{w}_l$, as well as $\mathbf{w}_j$ (respectively Δc_{p_j}) depend on the boundary conditions, expression (8) is inherently nonlinear. Therefore, it is computationally more expensive compared to the linear expression in (2). If $\mathbf{w}_l = \begin{bmatrix} 1 & 0 & 0 \end{bmatrix}^{\mathrm{T}}$, i.e. the free stream is assumed to be exclusively in x-direction, the analysis simplifies to the conventional case, with the lift $\mathbf{L}_l$ acting in the z-direction only.

In a last step, the lift vector $\mathbf{L}_l$ at the quarter chord is transformed to the reference point at the aerodynamic box centeroid.

$$\mathbf{P}_k^{\mathrm{aero}} = \mathbf{T}_{lk}^{\mathrm{T}} \, \mathbf{L}_l \tag{9}$$

As mentioned before the $k-\mathrm{set}$ has been extended to full 6 DOF to recover moments arising from the now directional lift vector.

2.2 Boundary Conditions: Differentiation Matrices

The boundary conditions for the Vortex Lattice Method are obtained with respect to a box reference point. Depending on the displacement, respectively motion of the reference point, the normal velocity $\mathbf{w}_j$ at the control point and velocity at the quarter chord point $\mathbf{w}_l$ need to be determined. The rotational displacement about the transverse axis contributes to the box angle of attack. The heaving motion, as well as rotational motion due to the offset of the reference point to the control point, also contribute to the effective box angle of attack.

These contributions can be accounted for by a differentiation wrt the x-direction, i.e. the change in slope θ_k, respectively wrt time for the normalized heaving motion $\dot{z}_k/U_\infty$ and pitching motion $\dot{\theta}_k/U_\infty$. These deformations and motions are represented in the vectors $\mathbf{u}_k$ and $\dot{\mathbf{u}}_k$. Thus, in matrix form this can be expressed as

$$\mathbf{w}_j = \mathbf{D^x}_{jk} \cdot \mathbf{u}_k \; + \; \mathbf{D^t}_{jk} \left(\tfrac{c_{ref}/2}{U_\infty} \right) \cdot \dot{\mathbf{u}}_k \tag{10}$$

The differentiation matrices are defined as

$$\mathbf{D^x}_{jk} = \begin{bmatrix} 0 & 0 & 0 & 0 & 1 & 0 \end{bmatrix} \tag{11}$$

and

$$\mathbf{D^t}_{jk} = -\tfrac{2}{c_{ref}} \begin{bmatrix} n_x & 0 & n_z & 0 & -c_j/4 & 0 \end{bmatrix}. \tag{12}$$

In order to account for camber and incidence, the quantities n_x and n_z are the components of the normal vector at the control point. The classical implementation omits the component in x-direction, i.e. $n_x = 0$ and $n_z = 1$ and merely treats camber as addition to the differential pressure. In the present implementation an in-plane motion results in an increased circulation.

The differentiation matrix $\mathbf{D^t}_{lk}$ is set up equivalently for the three translational DOFs at the quarter chord.

$$\mathbf{w}_l = \mathbf{D^t}_{lk} \left(\tfrac{c_{ref}/2}{U_\infty} \right) \cdot \dot{\mathbf{u}}_k \tag{13}$$

with

$$\mathbf{D^t}_{lk} = -\tfrac{2}{c_{ref}} \begin{bmatrix} 1 & 0 & 0 & 0 & 0 & 0 \\ 0 & 1 & 0 & 0 & 0 & -c_j/4 \\ 0 & 0 & 1 & 0 & c_j/4 & 0 \end{bmatrix} \tag{14}$$

Figure 2 illustrates the effects computed by equation (10) and (13).

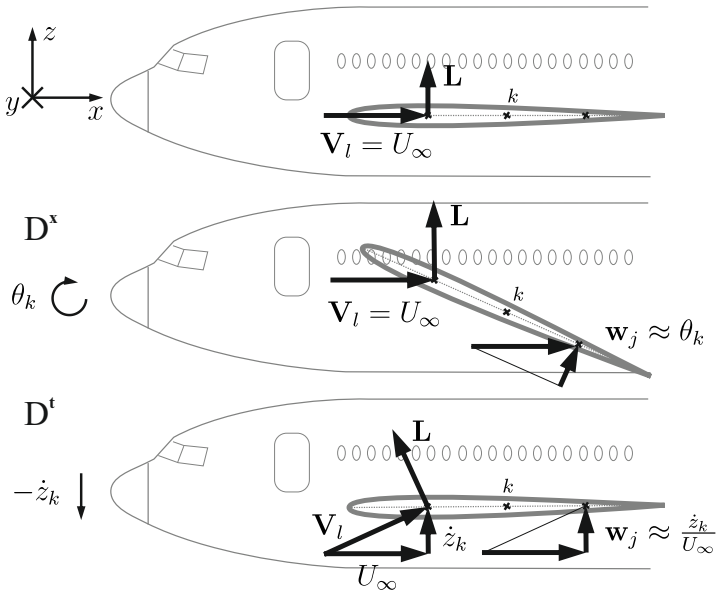

Figure 2: Illustration of the differentiation matrices $\mathbf{D^x}_{jk}$, $\mathbf{D^t}_{jk}$ and $\mathbf{D^t}_{lk}$

There is no matrix for $\mathbf{D^x}_{lk}$, as a steady deformation does not change the direction of flow. However, the heaving motion changes the direction of the lift vector. In the classical VLM implementation this contribution is neglected.

2.3 Induced Drag

Aerodynamic lift is generated by circulation Γ over the wing. Since the circulation distribution of a finite wing has to go to zero at the wing tips, a spanwise gradient in circulation results. Induced drag is generated by this spanwise change of the circulation of a 3D lifting surface, which leads to trailing vortices that are shed into the wake. The streamwise vorticity in the wake induces an additional downwash (15) on the wing, which turns the lift vector rearwards by the induced angle of attack (16). Figure 3 shows the the effect on an airfoil section of a finite wing.

Induced downwash is obtained by the integral equation:

$$w_i(y) = -\frac{1}{4\pi}\int_{-b/2}^{b/2} \frac{\mathrm{d}\Gamma(y_0)}{\mathrm{d}y}\frac{\mathrm{d}y_0}{y-y_0} \tag{15}$$

Using a small angle assumption, the induced angle of attack is then given by

$$\alpha_i(y) \approx \frac{-w_i(y)}{U_\infty}. \tag{16}$$

The overall induced drag can then be obtained by integrating over the wing span

$$D_i = \frac{1}{2}\rho U_\infty \int_{-b/2}^{b/2} \Gamma(y)\alpha_i(y)\ \mathrm{d}y. \tag{17}$$

Similarly, the total lift is obtained by

$$L = \rho U_\infty \int_{-b/2}^{b/2} \Gamma(y)\ \mathrm{d}y. \tag{18}$$

When comparing the integral equations, it can be seen that the lift (18) depends linearly on the overall circulation Γ, only. Whereas, in the drag integral (17), the induced angle of attack α_i is also a function of the circulation Γ, leading to the classical parabola shape of the drag polar.

To obtain the drag forces for the Vortex Lattice Method, there are two options:

- far field implementation:
  Solving the integral equations (17) and (18) in the so called Trefftz plane, which is located far downstream and perpendicular to the wake. The integration is carried out along the wake surface in this plane.
- near field implementation:
  Determining the induced downwash at the quarter-chord point of each box turning the local lift vectors as depicted in figure 3.

The near field implementation is very attractive, as the flexible aircraft equations of motion (23) require a distributed aerodynamic loading. One drawback of it is that it is somewhat sensitive to the discretization of the lifting surface.

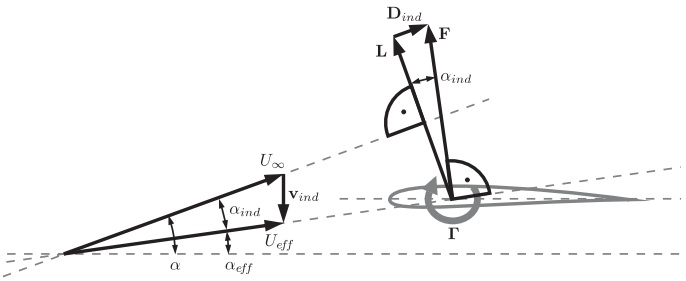

Figure 3: Illustration of induced drag and induced angle of attack

2.3.1 Near Field Induced Drag

The vorticity of the trailing vortices in the wake induces an additional downwash at the quarter chord of each box, which rotate the lift vector rearwards. The sum of the rearward component

of all boxes constitute the induced drag. To evaluate the induced velocities at the quarter chord point, once again the Biot-Savart Law is employed. The contribution of the bound vortex of the current box itself needs to be omitted, due to the singularity at zero distance. The three velocity components normalized by the free stream velocity are collected in the vector $\mathbf{w}_{l_{\text{ind}}}$. Similarly to eq. (1), this operation can be expressed as matrix equation.

$$\mathbf{w}_{l_{\text{ind}}} = \mathbf{A}_{lj} \frac{\Gamma_j}{U_\infty} \tag{19}$$

To build up the effective stream direction $\mathbf{w}_l$, the induced component $\mathbf{w}_{l_{\text{ind}}}$ is added to the free stream and motion induced components of equation (13). The subsequent force calculation in eq. (8) then includes the induced drag components.

2.3.2 Far Field Induced Drag

The evaluation of the far field is done by evaluation of eq. (17) in its discretized form. Once again the Biot-Savart Law is employed, but instead of calculating the downwash at the quarter chord, the induced velocity is evaluated on the wake surface far downstream in the so called Trefftz plane. The contributions of the individual box horseshoe vortices for each strip need to be summed up by multiplication of matrix $\mathbf{S}_{sj}$. The normalized velocity component perpendicular to the wake surface $\mathbf{w}_{s_{\text{ind}}}$ is then evaluated at the mid distance between these stripwise vortex pairs. The overall circulation of the wake strip is then multiplied with the perpendicular induced velocity and the wake strip width b_s. All wake strips are then summed up to the overall induced drag coefficient.

$$C_{D\,\text{FF}} = \frac{1}{S_{\text{ref}}} \sum_{n_s} b_s \cdot \mathbf{w}_{s_{\text{ind}}} \cdot \mathbf{S}_{sj} \frac{\Gamma_j}{U_\infty} \tag{20}$$

Equivalently, the overall lift is determined by a far field evaluation of eq. (18)

$$C_{L\,\text{FF}} = \frac{2}{S_{\text{ref}}} \sum_{n_s} b_s \cdot n_{z_s} \cdot \mathbf{S}_{sj} \frac{\Gamma_j}{U_\infty} \tag{21}$$

Similarly, the side force coefficient can be calculated in the far field

$$C_{Y\,\text{FF}} = \frac{2}{S_{\text{ref}}} \sum_{n_s} b_s \cdot n_{y_s} \cdot \mathbf{S}_{sj} \frac{\Gamma_j}{U_\infty} \tag{22}$$

The force components of each wake strip in the wind axis system are determined by n_{z_s} for the lift coefficient, respectively n_{y_s} for the side force coefficient.

2.4 Equations of Motion

The flexible aircraft structure is typically available as finite element model. A static reduction, known as Guyan reduction [15] is employed to reduce the aircraft components, such as wings, tails and fuselage along their loads reference axes. These structural points are denoted by the $g-$ set. The mass distribution is also given in this $g-\text{set}$ and a modal analysis is carried out. Only part of this modal basis is retained to further reduce the model size and associated computational cost. The modal Eigenvectors are given by $\mathbf{\Phi}_{gb}$ for the rigid body modes, respectively $\mathbf{\Phi}_{gf}$ for the flexible modes.

The equations of motion used are based on a "mean axes" formulation [16] including nonlinear rigid body motion as well as linear structural dynamics.

$$\begin{aligned}\begin{bmatrix}\mathbf{m}_b\left(\dot{\mathbf{V}}_b+\boldsymbol{\Omega}_b\times\mathbf{V}_b-\mathbf{T}_{bE}\,\mathbf{g}_E\right)\\ \mathbf{J}_b\dot{\boldsymbol{\Omega}}_b+\boldsymbol{\Omega}_b\times(\mathbf{J}_b\boldsymbol{\Omega}_b)\end{bmatrix}&=\boldsymbol{\Phi}_{gb}^{\mathrm{T}}\mathbf{P}_g^{\mathrm{ext}}(t)\\ \mathbf{M}_{ff}\ddot{\mathbf{u}}_f+\mathbf{B}_{ff}\dot{\mathbf{u}}_f+\mathbf{K}_{ff}\mathbf{u}_f&=\boldsymbol{\Phi}_{gf}^{\mathrm{T}}\mathbf{P}_g^{\mathrm{ext}}(t),\end{aligned}\tag{23}$$

where $\boldsymbol{\Phi}_{gb}$ is the rigid body modal matrix about the center of gravity and in directions as customary in flight mechanics, i.e x-forward, z-down. $\mathbf{V}_b$ and $\boldsymbol{\Omega}_b$ are the velocity, respectively angular velocity vectors in the body frame of reference. The matrix $\mathbf{T}_{bE}$ transforms the gravitational vector from an earth fixed (E) to the body fixed coordinate frame (b) as a function of Euler angles. The inertial tensor $\mathbf{J}_b$ and the aircraft mass $\mathbf{m}_b$ can be obtained from the 6×6 mass matrix $\mathbf{M}_{bb}=\boldsymbol{\Phi}_{gb}^{\mathrm{T}}\,\mathbf{M}_{gg}\,\boldsymbol{\Phi}_{gb}$. The flexible modal mass $\mathbf{M}_{ff}$ and stiffness $\mathbf{K}_{ff}$ are obtained accordingly.

The equations of motion are driven by the external forces $\mathbf{P}_g^{ext}$. Sources for these external loads are from the propulsion and the distributed aerodynamics described in the previous sections.

2.5 Interconnection of Aerodynamics with the Equations of Motion

The aerodynamic loads of eq. (9) are given in the $k-\mathrm{set}$ and have to be mapped to the structural degrees of freedom in the $g-\mathrm{set}$. The matrix connecting the displacements of these two grids is the so called spline matrix $\mathbf{T}_{kg}$.

$$\mathbf{u}_k=\mathbf{T}_{kg}\,\mathbf{u}_g\tag{24}$$

This mapping can be achieved by employing radial basis functions such as the Infinite Plate Spline (IPS) [17]. Important to note is that the spline has to be extended to all six degrees of freedom in the case of directional lift vectors.

The aerodynamic loads can be mapped back onto the structure with the transpose of the spline matrix, based on the principle of virtual work.

$$\mathbf{P}_g^{\mathrm{aero}}=\mathbf{T}_{kg}^{\mathrm{T}}\,\mathbf{P}_k^{\mathrm{aero}}\tag{25}$$

The deflections of the aerodynamic degrees of freedom can then be expressed as

$$\mathbf{u}_k=\boldsymbol{\Phi}_{kx}\mathbf{u}_x+\mathbf{T}_{kg}\,\boldsymbol{\Phi}_{gf}\mathbf{u}_f,\tag{26}$$

where $\mathbf{u}_x$ denotes control surface deflections with $\boldsymbol{\Phi}_{kx}$ defining a rotation about a hinge vector of the aerodynamic boxes belonging to the individual control surfaces. Accordingly, the aerodynamic box velocities are given by

$$\dot{\mathbf{u}}_k=\boldsymbol{\Phi}_{kx}\dot{\mathbf{u}}_x+\mathbf{T}_{kg}\,\boldsymbol{\Phi}_{gf}\dot{\mathbf{u}}_f+\mathbf{T}_{kg}\,\boldsymbol{\Phi}_{gb}\dot{\mathbf{u}}_b.\tag{27}$$

The vector $\dot{\mathbf{u}}_b$ denotes the rigid body velocity components and rates about the center of gravity in the body axis system. The aerodynamic grid deflections and motions are then used in eq. (10) and (13) to obtain the aerodynamic loads.

2.6 Trimming and Linearization

The overall equations of motion with the aerodynamic forcing terms represent a nonlinear system of ordinary differential equations:

$$\begin{aligned} \dot{x} &= f(x, u) \\ y &= g(x, u) \end{aligned} \tag{28}$$

The starting conditions for a dynamic manoeuvre have to be determined, such that the aircraft is in an equilibrium state, i.e. all forces and moments must be balanced. The most prominent equilibrium state is the horizontal flight, but also any other flight state that constitutes a solution to the system is valid.

Mathematically, the nonlinear system of equations (28) has to be solved, where the states x, state derivatives $\dot{x}$, inputs u and outputs y can be either free or constraint variables. In order to compute a valid solution, the number of free variables has to equal the number of equations of the given system. The inputs are generally the control surfaces deflections, which are allocated to issue roll, pitch, yaw commands and the engine thrust setting. The outputs are chosen according to the requirements for the flight condition, e.g. angle of attack α, sideslip angle β, Mach number Ma, and load factor N_z. When the constraints are set accordingly, a trim routine based on the `MINPACK` library [18], solves the system. The trim solution defines the initial conditions x_0 and u_0 for the simulation.

When the nonlinear aircraft model is linearized around the given trim state, a linear state space system can be obtained. An eigenvalue analysis of the system matrix yields the root locus of the flexible and flight mechanical modes with their associated damping ratios and frequencies.

3 RESULTS: OPTIMAL CONTROL SURFACE SCHEDULING

A flexible aircraft model, which lends itself to demonstrate wing shaping control is the FLEXOP demonstrator aircraft T-FLEX [19]. The aircraft features a high aspect ratio and multiple trailing edge control surfaces distributed over the wing span. The original aircraft is equipped with four ailerons per wing. To allow for a finer granularity, each aileron has been split fourways for the simulation model used in this study, resulting in overall 16 ailerons per wing. The VLM model of the wing is depicted in figure 4. Not shown is a V-tail equipped with two elevators per empennage surface, which allow for pitch and yaw control. The fuselage is not modelled aerodynamically and no empirical corrections for additional drag components have been employed in the simulation model. The propulsion system is based on a single jet engine mounted on top of the fuselage. The external propulsion forces are introduced into the structure accordingly, including the pitching moment contribution.

The use cases demonstrate the capabilities of the proposed modelling approach with regards to performance improvement through lift re-distribution as well as manoeuvre load alleviation, by optimal control surface deflection. Furthermore, the effect on the phugoid flight mechanical mode of the present VLM is contrasted to the classical implementation.

All applications are be based on a flexible aircraft model with nonlinear equations of motion based on mean axes constraints, as described in the previous sections. The model is trimmed by a nonlinear solver for horizontal flight condition or a pull up manoeuvre, specified by a given load factor. Optionally a linearized state space model can be obtained to assess the root loci.

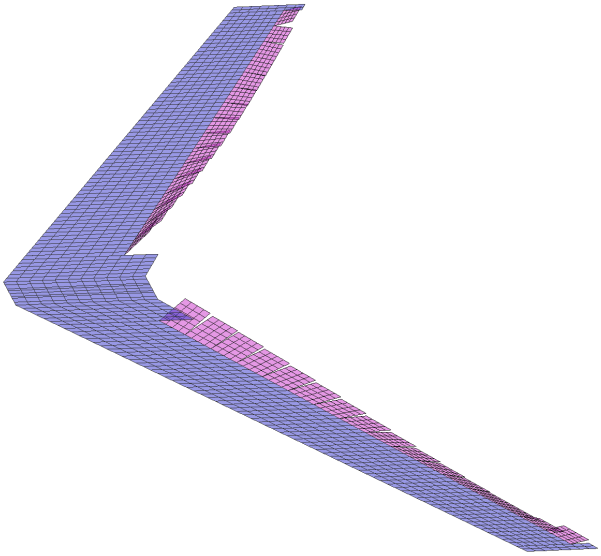

Figure 4: Flexible aircraft model with high aspect ratio wing and multiple tailing edge control surfaces

3.1 Performance Improvement through Wing Shape Control

An optimal (preferably elliptic) lift distribution ensures low induced drag. During the mission of the aircraft, the fuel stored in the wings is consumed and therefore the mass properties change. Hence, the lift distribution changes due to aeroelastic effects. Usually, aircraft are designed for typical intermediate mass cases. However, away from this design point, either very heavy at the beginning, or very light at the end of the mission, the lift distribution is not optimal anymore. With adequate control surfaces available, the lift distribution can be modified to reduce the detrimental effect on the performance.

The T-FLEX aircraft does not have fuel tanks in the wing and due to the comparatively small fuel tank, the weight of the aircraft is only changing minimally during a test flight. Therefore, the aircraft speed is varied over a wide range to obtain off-design lift coefficients.

The objective is to minimize the required thrust in a trimmed horizontal flight condition for a given speed, by symmetrically deflecting the 16 trailing edge control surfaces per wing. To demonstrate the effectiveness of the Wing Shape Control (WSC), the results are compared to the induced drag values of the reference case without control surface deflections. It should be noted that the drag values also include the trim drag component of the overall flexible aircraft. Hence, the optimal wing lift-distribution might differ from an elliptical shape, since the pitching moment has to be balanced by tail surface deflections. In that regard the obtained values correspond to an overall optimum of the entire flexible airframe in a trimmed flight condition.

One evaluation of a trimmed flight condition takes about 1.1 s. For the 16 symmetrically deflected control surfaces as optimization parameters, around 800 iterations are needed to a reach a flight state with minimal required thrust. A paralellized run for the 17 flight points between 35 and 75 m/s took approximately 20 minutes. The resulting control surface deflections of the 16 ailerons for the wing shape control over the wing span are depicted in figure 5.

The associated drag polar is drawn in figure 6. The polar for the reference case is drawn in orange, the drag reduced polar with wing shape control in blue. The solid line are determined using the distributed near field implementation, which is used for trimming the flexible aircraft. The dashed lines are the integral far field evaluations in Trefftz plane of the total drag coefficient.

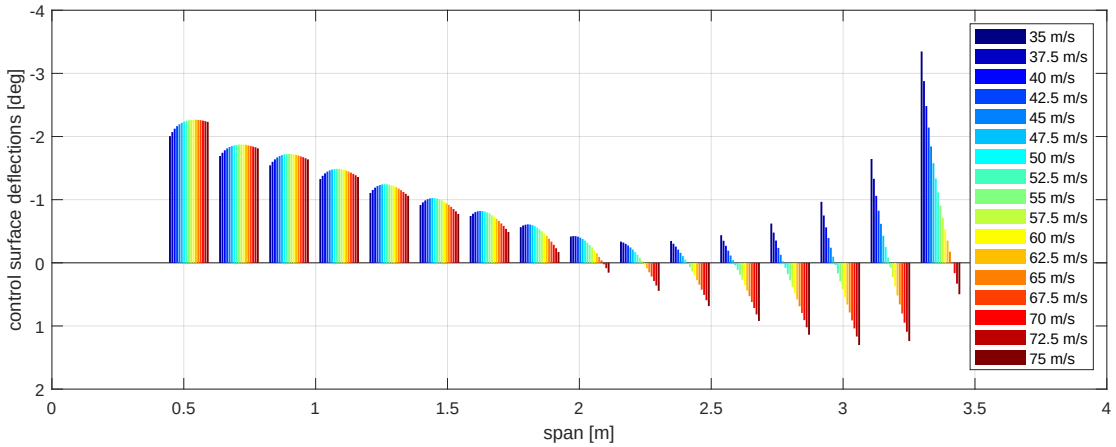

Figure 5: Optimal control surface deflections for different velocities

While a difference between near and far field evaluation exists, the relative drag reduction of the wing shape control is nearly the same.

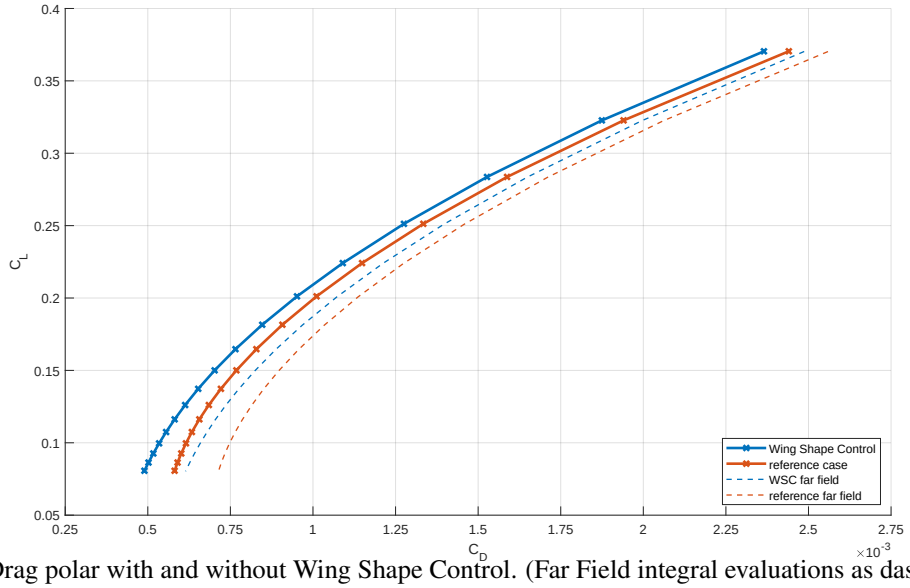

Figure 6: Drag polar with and without Wing Shape Control. (Far Field integral evaluations as dashed lines)

The lift and drag coefficients along with the relative drag improvements are summarized in table 1. The drag coefficients are represented in drag counts, i.e. $C_D \times 10^4$ for better readability.

V_{TAS} [m/s]	C_L	$C_{Di} \times 10^4$ ref.	$C_{Di} \times 10^4$ WSC	drag reduction ratio	$C_{Di} \times 10^4$ ref. (Far Field)	$C_{Di} \times 10^4$ WSC (Far Field)
35.0	0.37043	24.405	23.651	1.0319	25.59	24.87
37.5	0.32271	19.402	18.745	1.0351	20.61	19.959
40.0	0.28364	15.876	15.268	1.0398	17.101	16.48
42.5	0.25126	13.34	12.754	1.046	14.579	13.964
45.0	0.22412	11.486	10.902	1.0536	12.736	12.113
47.5	0.20115	10.109	9.516	1.0624	11.368	10.728
50.0	0.18154	9.0741	8.4635	1.0721	10.341	9.6771
52.5	0.16467	8.2866	7.6536	1.0827	9.5607	8.8693
55.0	0.15004	7.6816	7.0229	1.0938	8.9623	8.2411
57.5	0.13728	7.2129	6.526	1.1053	8.4997	7.747
60.0	0.12608	6.8472	6.1305	1.1169	8.1399	7.3545
62.5	0.1162	6.5602	5.8124	1.1286	7.8585	7.0397
65.0	0.10743	6.3338	5.5541	1.1404	7.6379	6.7849
67.5	0.099623	6.1547	5.3424	1.1521	7.4645	6.5768
70.0	0.092635	6.0128	5.1671	1.1637	7.3284	6.4053
72.5	0.086358	5.9003	5.0208	1.1752	7.2219	6.2628
75.0	0.080698	5.8113	4.8974	1.1866	7.1391	6.1433

Table 1: Lift and induced drag coefficients with and without Wing Shape Control. (Note: drag is given in drag counts $C_D \times 10^4$)

3.2 Manoeuvre Load Alleviation

For certification of an aircraft, it has to be demonstrated that its structure can withstand the loads acting on it without damage. In order to design the structure accordingly, a so called loads envelope has to be computed. One of the critical load conditions comprising the loads envelope is the symmetrical pull up manoeuvre. For large transport aircraft, this condition is specified in the paragraphs CS 25.331 and CS 25.333 of the CS-25 issued by the EASA [20]. One way of reducing the resulting wing root bending moment and hence the structural weight of the wing, is to shift the center of the lift distribution inboard by deflecting the control surfaces. This function is known as Manoeuvre Load Alleviation (MLA).

The objective is to find the optimal control surface scheduling to minimize the wing root bending moment. The aircraft model of the T-FLEX demonstrator is used and extended with load station outputs for bending and torsion at the wing root. Since the design weight of the demonstrator aircraft is small (around 65 kg), the design load factor is significantly higher. For this study a positive load factor of $N_z = 5.0$ was chosen.

The aircraft model is trimmed for a pull-up manoeuvre with the resulting pitch rate to reach the desired load factor. The maximum deflections for the 16 wing trailing edge surfaces were set to be ± 10 deg. Such a setup requires a constraint optimization with the objective function minimizing the resulting wing root bending moment by symmetric deflection of the trailing edge control surfaces. Ultimately, to reduce the root bending moment the center of lift has to be shifted inboard. Physically, that means that the inboard lift has to be increased by deflecting the inner control surfaces downward, while the outer control surfaces have to decrease local lift by upward deflection.

As this particular constraint optimization problem showed that the control surfaces were always deflected to their respective positive and negative limits, a different strategy was chosen. To find the optimal spanwise cross-over location, where full downward deflection changes to full upward deflection of the trailing edge control surfaces, 17 discrete configurations were examined. The control suface deflections of theses configurations are given in table 2. The reference case is without any MLA function, i.e. no deflection of the control surfaces. For configuration 0 all ailerons are deflected upwards -10 deg. The configs 1 through 16 consecutively deflect more control surfaces from inboard to outboard downwards to 10 degrees, until for configuration 16 all ailerons are deflected downwards.

config	ail 1	ail 2	ail 3	ail 4	ail 5	ail 6	ail 7	ail 8	ail 9	ail 10	ail 11	ail 12	ail 13	ail 14	ail 15	ail 16
reference	0.0	0.0	0.0	0.0	0.0	0.0	0.0	0.0	0.0	0.0	0.0	0.0	0.0	0.0	0.0	0.0
0	-10.0	-10.0	-10.0	-10.0	-10.0	-10.0	-10.0	-10.0	-10.0	-10.0	-10.0	-10.0	-10.0	-10.0	-10.0	-10.0
1	+10.0	-10.0	-10.0	-10.0	-10.0	-10.0	-10.0	-10.0	-10.0	-10.0	-10.0	-10.0	-10.0	-10.0	-10.0	-10.0
2	+10.0	+10.0	-10.0	-10.0	-10.0	-10.0	-10.0	-10.0	-10.0	-10.0	-10.0	-10.0	-10.0	-10.0	-10.0	-10.0
3	+10.0	+10.0	+10.0	-10.0	-10.0	-10.0	-10.0	-10.0	-10.0	-10.0	-10.0	-10.0	-10.0	-10.0	-10.0	-10.0
4	+10.0	+10.0	+10.0	+10.0	-10.0	-10.0	-10.0	-10.0	-10.0	-10.0	-10.0	-10.0	-10.0	-10.0	-10.0	-10.0
5	+10.0	+10.0	+10.0	+10.0	+10.0	-10.0	-10.0	-10.0	-10.0	-10.0	-10.0	-10.0	-10.0	-10.0	-10.0	-10.0
6	+10.0	+10.0	+10.0	+10.0	+10.0	+10.0	-10.0	-10.0	-10.0	-10.0	-10.0	-10.0	-10.0	-10.0	-10.0	-10.0
7	+10.0	+10.0	+10.0	+10.0	+10.0	+10.0	+10.0	-10.0	-10.0	-10.0	-10.0	-10.0	-10.0	-10.0	-10.0	-10.0
8	+10.0	+10.0	+10.0	+10.0	+10.0	+10.0	+10.0	+10.0	-10.0	-10.0	-10.0	-10.0	-10.0	-10.0	-10.0	-10.0
9	+10.0	+10.0	+10.0	+10.0	+10.0	+10.0	+10.0	+10.0	+10.0	-10.0	-10.0	-10.0	-10.0	-10.0	-10.0	-10.0
10	+10.0	+10.0	+10.0	+10.0	+10.0	+10.0	+10.0	+10.0	+10.0	+10.0	-10.0	-10.0	-10.0	-10.0	-10.0	-10.0
11	+10.0	+10.0	+10.0	+10.0	+10.0	+10.0	+10.0	+10.0	+10.0	+10.0	+10.0	-10.0	-10.0	-10.0	-10.0	-10.0
12	+10.0	+10.0	+10.0	+10.0	+10.0	+10.0	+10.0	+10.0	+10.0	+10.0	+10.0	+10.0	-10.0	-10.0	-10.0	-10.0
13	+10.0	+10.0	+10.0	+10.0	+10.0	+10.0	+10.0	+10.0	+10.0	+10.0	+10.0	+10.0	+10.0	-10.0	-10.0	-10.0
14	+10.0	+10.0	+10.0	+10.0	+10.0	+10.0	+10.0	+10.0	+10.0	+10.0	+10.0	+10.0	+10.0	+10.0	-10.0	-10.0
15	+10.0	+10.0	+10.0	+10.0	+10.0	+10.0	+10.0	+10.0	+10.0	+10.0	+10.0	+10.0	+10.0	+10.0	+10.0	-10.0
16	+10.0	+10.0	+10.0	+10.0	+10.0	+10.0	+10.0	+10.0	+10.0	+10.0	+10.0	+10.0	+10.0	+10.0	+10.0	+10.0

Table 2: Control surface deflections of the discrete MLA configurations

Note, that the wing root bending moment can be reduced in lieu of tail moments and a suitable strategy for finding the overall minimum of the structural weight has to be found. The wing

root torsion moment is an indicator of the pitching moment contribution of the tail needed to balance the aircraft, i.e. how much of the wing load is traded for tail loads. Hence, the torsion moment is also monitored.

The results of the pull-up manoeuvres are shown in figure 7. The wing root bending moment in blue with the left y-axis and wing root torsion moment in orange with the right y-axis. The dashed lines represent the reference case, where no MLA is employed.

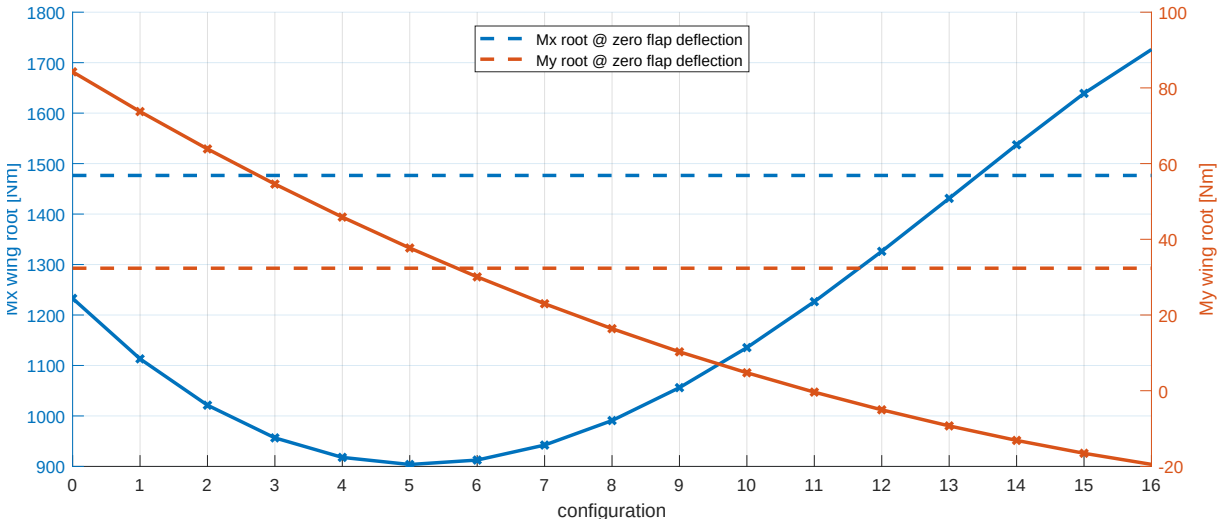

Figure 7: Wing root bending and torsion moment for 17 different MLA configurations

The minimum wing root bending moment is achieved, when the inner 5 ailerons are deflected downward and the remaining 11 ailerons are deflected upwards. Incidentally, this configuration hardly changes the root torsion moment compared to the reference configuration without an MLA function. This implies that using this MLA control allocation will change the pitching moment only minimally and no significant penalty for the tail loads are incurred.

The objective function for this study was solely the wing root bending moment. If overall structural weight from a structural sizing procedure is formulated as objective, the control surface setting might look different as the spanwise distribution of the bending moment becomes more important.

3.3 Flight Dynamic Modes

Flight mechanical modes are associated with the dynamic characteristics of an aircraft. They can be divided in lateral and longitudinal modes. The lateral modes are the oscillatory dutch roll mode and the aperiodic roll subsidence and spiral mode. The longitudinal modes are comprised of the short period mode with rapid changes in angle of attack and the so called phugoid.

The phugoid mode is an aircraft motion in which the vehicle pitches up and climbs while slowing down, which in turn leads to a pitch down and a speed increase during the descend with only minor changes in angle of attack. This exchange of altitude and airspeed is heavily influenced by the drag polar of the aircraft. Therefore, the physical modelling of the induced drag enhances the predictive capabilities of the model significantly. As the phugoid mode might be lightly damped or even mildly unstable, it is an important consideration in flight control law design.

The simulation model is used in its current reference configuration, i.e. no augmented control surface deflections and trimmed for horizontal flight condition. The flight points considered are between 25 and 75 m/s. The model is linearized around the trim states and the poles are computed by an eigenvalue analysis of the system matrix. The phugoid mode is identified by examining the eigenvectors for the typical trade-off between speed and altitude. The pole migration of the identified complex conjugate pair of the phugoid mode can then be presented either in a root locus plot or as frequency and damping ratio versus flight speed.

This procedure has been applied to a model using the present VLM scheme with directional lift including near field induced drag terms and to a classical implementation using a lift force acting in the body z-direction only. The damping ratio ζ_{phugoid} and the frequency ω_{phugoid} of phugoid

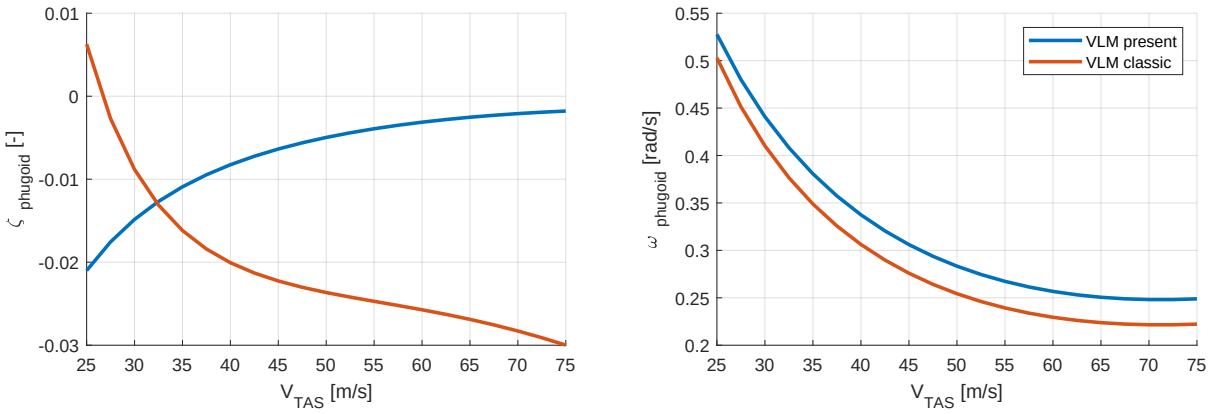

Figure 8: Phugoid damping and frequency versus flight speed

mode is depicted in figure 8. The frequencies are very similar between the implementations. The damping ratios however even show an opposing trend, where the present VLM in blue shows a mildly unstable behaviour that approaches neutral stability for increasing speed. The classical implementation in orange becomes even more unstable as the flight speed increases. A final validation of this behavior, respectively verification with other proven methods is still pending.

4 SUMMARY AND CONCLUSIONS

The modelling approach proposed in [1] covered loads analysis as well as flight dynamics simulations. In this paper the approach has been extended to the field of performance by accounting for induced drag to allow for the design of active control functions regarding wing shape control for off-design points during the mission.

Previously, 3D panel methods were used for modelling of the relevant in-plane forces for flight dynamics simulations [3, 5]. As an alternative the Vortex Lattice Method was extended in the present paper to account for directional lift vectors and induced drag terms. This has been accomplished by the use of a cross product form of the Kutta Joukowski Law instead of the simple scalar multiplication, that is typical for many commercial aeroelastic codes. The matrix based formulation of the Aerodynamic Influence Coefficients and the boundary conditions is preserved, allowing for a seamless integration in the integral modelling approach. The influence of the wake induced velocity at the bound vortex location, i.e. the induced drag of the flexible aircraft is also included. This significantly enhances the capabilities of the model for flight dynamics and performance applications.

A simulation model of the T-FLEX demonstrator aircraft, which is used for flight testing in the EU project FLiPASED, was set up with the present VLM implementation. An optimization was performed to obtain optimal control surface scheduling to minimize induced drag for different flight points. These optimized control surface settings will be used in test flights in conjunction with a thrust measurement system for validation.

Furthermore, optimal control surface scheduling for active Manoeuvre Load Alleviation control functions were determined by minimizing the wing root bending moment with the same simulation model.

Linearization of the current model and subsequent eigenvalue analysis of the LTI representation, allowed for assessment of the root loci of the flexible dynamic aircraft modes. In particular the phugoid mode was of interest, as it is heavily dependent on the previously unmodelled drag. The development of the damping ratios and frequencies of the phugoid mode were shown for different flight speeds.

The present modelling approach was shown to be suitable for optimzation of control surface scheduling supporting control law design of load alleviation and wing shape control functions, as well as flight dynamics and manoeuvre load analyses.

5 ACKNOWLEDGEMENTS

The research leading to these results is part of the FLiPASED project. This project has received funding from the European Unions Horizon 2020 research and innovation program under grant agreement No. 815058.

6 REFERENCES

[1] Kier, T. M. (2018). An integrated modelling approach for flight dynamics, manoeuvre- and gust-loads analysis. In *59th AIAA/ASCE/AHS/ASC Structures, Structural Dynamics, and Materials Conference, 8-12 January 2018, Kissimmee, FL, USA*, AIAA 2018-2209. AIAA. doi:10.2514/6.2018-2209.

[2] Kier, T. M., Leitner, M., Özge Süelözgen, et al. (2019). An integrated flexible aircraft model for optimization of lift distributions. In *AIAA Scitech 2019 Forum*. American Institute of Aeronautics and Astronautics. doi:10.2514/6.2019-2039.

[3] Kier, T. M. (2015). Integrated Flexible Dynamic Maneuver Loads Models based on Aerodynamic Influence Coefficients of a 3D Panel Method. In *56th AIAA/ASCE/AHS/ASC Structures, Structural Dynamics, and Materials Conference, 5-9 January 2015, Kissimmee, FL, USA*, AIAA 2015-0185. AIAA. doi:10.2514/6.2015-0185.

[4] Kier, T. M., Verveld, M. J., and Burkett, C. W. (2015). Integrated Flexible Dynamic Loads Models Based on Aerodynamic Influence Coefficients of a 3D Panel Method. In *International Forum on Aeroelasticity and Structural Dynamics*, IFASD-2015-179.

[5] Kier, T. M. (2017). An Integrated Model for Lateral Gust Loads Analysis and Dutch Roll Flight Dynamics using a 3D Panel Method. In *International Forum on Aeroelasticity and Structural Dynamics*, IFASD-2017-107.

[6] Kolonay, R. M. and Eastep, F. E. (2006). Optimal scheduling of control surfaces on flexible wings to reduce induced drag. *Journal of Aircraft*, 43(6), 1655–1661. doi: 10.2514/1.14604.

[7] Eller, D. and Heinze, S. (2005). Approach to induced drag reduction with experimental evaluation. *Journal of Aircraft*, 42(6), 1478–1485. doi:10.2514/1.11713.

[8] Ting, E., Chaparro, D., Nguyen, N., et al. (2018). Optimization of Variable-Camber Continuous Trailing-Edge Flap Configuration for Drag Reduction. *Journal of Aircraft*, 55(6), 2217–2239. doi:10.2514/1.c034810.

[9] Pusch, M., Kier, T. M., Tang, M., et al. (2022). Advanced gust load alleviation using dynamic control allocation. In *AIAA SCITECH 2022 Forum*. American Institute of Aeronautics and Astronautics. doi:10.2514/6.2022-0439.

[10] Hofstee, J., Kier, T., Cerulli, C., et al. (2003). A Variable, Fully Flexible Dynamic Response Tool for Special Investigations (VarLoads). In *International Forum on Aeroelasticity and Structural Dynamics*.

[11] Hedman, S. (1965). Vortex Lattice Method for Calculation of Quasi Steady State Loadings on Thin Elastic Wings. Tech. Rep. Report 105, Aeronautical Research Institute of Sweden.

[12] Pistolesi, E. (1937). Betrachtungen über die gegenseitige Beeinflussung von Tragflügelsystemen. In *Gesammelte Vorträge der Hauptversammlung 1937 der Lilienthal Gesellschaft*.

[13] Rodden, W. P., Harder, R. L., and Bellinger, E. D. (1979). Aeroelastic Addition to NASTRAN. Tech. Rep. NASA CR-3094, NASA.

[14] Kier, T. M. and Looye, G. H. N. (2009). Unifying Manoeuvre and Gust Loads Analysis. In *International Forum on Aeroelasticity and Structural Dynamics*, IFASD-2009-106.

[15] Guyan, R. J. (1965). Reduction of stiffness and mass matrices. *Journal of Aircraft*, 3(2), 380. doi:10.2514/3.2874.

[16] M. R. Waszak and D. K. Schmidt (1988). Flight Dynamics of Aeroelastic Vehicles. *Journal of Aircraft*, 25(6), 563–571. doi:10.2514/3.45623.

[17] Harder, R. and Desmarais, R. (1972). Interpolation Using Surface Splines. *Journal of Aircraft*, 9(2), 189–191. doi:10.2514/3.44330.

[18] Moré, J. J., Garbow, B. S., and Hillstrom, K. E. (1980). User Guide for MINPACK-1. Tech. Rep. ANL-80-74, Argonne National Laboratory.

[19] Wüstenhagen, M., Kier, T., Meddaikar, Y. M., et al. (2018). Aeroservoelastic Modeling and Analysis of a Highly Flexible Flutter Demonstrator. In *2018 Atmospheric Flight Mechanics Conference*. American Institute of Aeronautics and Astronautics. doi:10.2514/6.2018-3150.

[20] European Aviation Safety Agency (2010). *Certification Specifications for Large Aeroplanes CS-25*, vol. Subpart C - Structure. EASA.

COPYRIGHT STATEMENT